

Improved surface charge and corrosion resistance at the near-nanocrystalline chromium/nano-bilayer oxide interface in advanced thin dense chromium coatings

Rahimi, Ehsan; Nijdam, Thijs; Jahagirdar, Adwait; Broitman, Esteban; Mol, Arjan

DOI

[10.1016/j.apsusc.2025.162504](https://doi.org/10.1016/j.apsusc.2025.162504)

Publication date

2025

Document Version

Final published version

Published in

Applied Surface Science

Citation (APA)

Rahimi, E., Nijdam, T., Jahagirdar, A., Broitman, E., & Mol, A. (2025). Improved surface charge and corrosion resistance at the near-nanocrystalline chromium/nano-bilayer oxide interface in advanced thin dense chromium coatings. *Applied Surface Science*, 689, Article 162504. <https://doi.org/10.1016/j.apsusc.2025.162504>

Important note

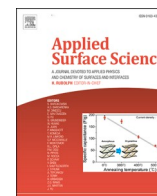
To cite this publication, please use the final published version (if applicable). Please check the document version above.

Copyright

Other than for strictly personal use, it is not permitted to download, forward or distribute the text or part of it, without the consent of the author(s) and/or copyright holder(s), unless the work is under an open content license such as Creative Commons.

Takedown policy

Please contact us and provide details if you believe this document breaches copyrights. We will remove access to the work immediately and investigate your claim.



Full Length Article

Improved surface charge and corrosion resistance at the near-nanocrystalline chromium/nano-bilayer oxide interface in advanced thin dense chromium coatings

Ehsan Rahimi^{a,*}, Thijs Nijdam^b, Adwait Jahagirdar^b, Esteban Broitman^b, Arjan Mol^a

^a Delft University of Technology, Department of Materials Science and Engineering, Mekelweg 2, 2628 CD Delft, the Netherlands

^b SKF Research & Technology Development, 3992AE Houten, the Netherlands

ARTICLE INFO

Keywords:

Thin dense chromium
Near-nanocrystalline
Surface charge resistance
Corrosion resistance
Kelvin probe force microscopy
Vertical differential charging
Effective work function

ABSTRACT

Chromium coatings, famed for their superior wear and corrosion resistance, are a critical component in countless industrial processes. However, the longevity of these coatings in aggressive corrosive environments continues to be a significant hurdle, even with recent advances in deposition technology and microstructural improvements. An advanced thin dense chromium (TDC) coating, with a near-nanocrystalline structure and unique morphology, naturally forms a non-conductive nano-bilayer oxide. This passive and protective layer effectively moderates electrical charge transfer, offering superior corrosion resistance. X-ray photoelectron spectroscopy (XPS) shows significant Cr³⁺ oxide layer formation, distinguished by multiplet splitting, after 7 days in a 0.6 M NaCl solution. The unique characteristics of this non-conductive bilayer oxide structure promote its growth and densification, leading to vertical differential charging in the O1s electron energy region. This effect arises from the enhanced resistivity of the oxide layer. Electrochemical impedance spectroscopy (EIS) confirmed these findings, showing a substantial increase in charge transfer resistance at the chromium metal/bilayer oxide interface, reaching 1.01 MΩ. Scanning Kelvin probe force microscopy (SKPFM) analysis shows that both TDC nodules and their boundaries exhibit high surface potential and work function. However, after exposure to NaCl media, these values are moderately reduced, likely due to diminished electrical surface charge distribution.

1. Introduction

Advanced surface protection and functionalization techniques remain the most effective strategies for preventing corrosion processes in electrochemically active metals and alloys, particularly steel families, in harsh, corrosive environments [1–3]. The utilization of transition metals that spontaneously form protective nano-scale oxide films with semiconductor properties is remarkably crucial in enhancing the durability and performance of these materials, thereby significantly extending their operational lifespan [4–6]. The chromium-functionalized coatings have consistently been regarded as a top-tier solution in protective strategies, particularly for applications demanding exceptional corrosion resistance [7–9]. The bilayer thin structure of the chromium passive film, comprised of a compact Cr₂O₃ inner layer and an outer Cr(OH)₃ layer, develops naturally and serves as a robust barrier, preventing aggressive ions (e.g., Cl⁻) from triggering localized corrosion [10,11]. The pseudo-inert passive film, with its p-

type semiconductor characteristics [12,13], requires a pristine crystalline structure of metallic chromium along with a well-defined surface morphology [14]. Together, these features synergistically optimize corrosion resistance and reduce electrochemical activity at the solid/liquid interface. As a result, considerable research has been devoted to advancing chromium electroplating technologies by refining microstructural attributes, including optimizing structure, crystal size, surface morphology, porosity [15,16], and especially formed pinholes and microcracks [14,17,18]. These efforts also focus on enhancing mechanical properties and improving chemical stability to achieve durable corrosion resistance over both short- and long-term periods [7,19]. To address these needs, we proposed Thin Dense Chromium (TDC), an advanced thin chromium coating with a completely crack-free deposit, hierarchically nodular texture, and a near-nanocrystalline, compact structure. In this investigation, we employ a diverse set of advanced techniques to uncover specific insights into the dense, near-nanocrystalline structure of TDC coatings. X-ray photoelectron

* Corresponding author.

E-mail address: e.rahimi-2@tudelft.nl (E. Rahimi).

<https://doi.org/10.1016/j.apsusc.2025.162504>

Received 6 December 2024; Received in revised form 8 January 2025; Accepted 20 January 2025

Available online 21 January 2025

0169-4332/© 2025 The Author(s). Published by Elsevier B.V. This is an open access article under the CC BY license (<http://creativecommons.org/licenses/by/4.0/>).

spectroscopy (XPS) is utilized to analyze the electronic structure, chemical composition, and oxidation states of the native and water-formed oxide film on TDC coating. While Atomic force microscopy coupled by scanning Kelvin probe force microscopy (SKPFM) reveals the localized surface electronic properties on the nanometer oxide film. Additionally, AC/DC multi-electrochemical analyses elucidate the electrochemical behavior and the dynamics of the bilayer nano-oxide formation at the metallic Cr/oxide/electrolyte interface.

2. Experimental procedure

2.1. Materials

In this study, we employed a proprietary thin dense chromium (TDC) coating process developed and commercialized by SKF [20–22], branded as Endurakote® [23]. The coating was electrodeposited onto substrates made of 52,100 bearing steel with dimensions of 15 mm × 25 mm × 5 mm, which consists of 0.98 %–1.10 % carbon, 1.30 %–1.60 % chromium, 0.15 %–0.30 % silicon, and 0.25 %–0.45 % manganese, along with trace amounts of sulfur (≤0.025 %) and phosphorus (≤0.025 %). The coating process begins with degreasing the workpieces in a heated alkaline solution, followed by surface preparation through etching or mild abrasive powder blasting. Before the electroplating procedure, the carbon steel surface displayed an arithmetic average roughness (Ra) of 150 nm, with a deviation of ±30 nm. The components are then immersed in a chromium acid electrolyte (Cr(VI)), where potassium dichromate acts as a catalyst. This facilitates the formation of a thin chromium layer with the desired surface properties, achieved by applying a lower current density and reducing the coating duration. Finally, the process concludes with cleaning and preservation to ensure the integrity and durability of the coating. TDC is specifically designed to enhance hardness and wear resistance. Furthermore, the coating offers superior anti-corrosion properties due to its dense, micro-crack-free microstructure [21]. Its engineered surface topography also influences frictional behavior, making TDC coatings ideal for applications demanding precise friction control. In bearing applications, the coating thickness is meticulously maintained at approximately 5 μm, ensuring optimal surface functionality and performance.

2.2. SEM, EDXS and EBSD

The surface morphology and microstructure of the TDC coating were examined using a scanning electron microscope (Teneo, FEI™) equipped with secondary electron (SE) and backscatter electron (BSE) detectors. The SEM was operated at an accelerating voltage of 5 kV, a beam current of 0.4 nA, and a working distance of 10 mm. EBSD analysis was conducted on cross-sectional TDC samples using a 15 kV accelerating voltage, 6.4 nA beam current, a scanning step size of 40 nm, and a 10 mm working distance.

2.3. AFM, and SKPFM

To explore the surface topography and electronic surface potential changes of the TDC coating before and after exposure to 0.6 M NaCl, AFM, and SKPFM measurements were conducted using a Bruker Dimension Edge™ system. A PtIr coated antimony (n)-doped silicon tip (SCM-Pit-V2 probe) with a 25 nm radius and 10–15 μm height was employed. Measurements were performed in dual-scan mode: topography was captured in dynamic (tapping) mode during the first scan, while surface potential was recorded at a 100 nm lift height during the second, following the topography contour. Experiments were conducted ex-situ in ambient air (22 °C, ~30 % RH), using a pixel resolution of 512 × 512, a zero DC bias, and a scan frequency of 0.3 Hz.

2.4. XPS

X-ray photoelectron spectroscopy (XPS) was utilized in this study to investigate the chemical states of the bilayer oxide on the TDC coating before and after exposure to the NaCl solution. The measurements were conducted using a PHI Versaprobe II spectrometer equipped with a monochromatic Al Kα X-ray source (1486.6 eV). The binding energy scale was calibrated against Cu 2p3/2 (932.62 ± 0.1 eV) and Au 4f7/2 (83.96 ± 0.1 eV) standards. Spectra were collected at a take-off angle of 45° with a 200 μm beam diameter, operating at an irradiation power of 49.6 W. The sample, a TDC-coated flat 52100 steel plate (25 × 10 × 4 mm), was mounted on the specimen holder using double-sided tape for electrical insulation. A combined low-energy electron and ion beam charge neutralization system was employed to mitigate charging effects, and the settings were verified with a PET reference sample, achieving an O=C–O C1s peak FWHM of less than 0.85 eV.

Survey scans were carried out across the energy range of 1400–0 eV, with a pass energy of 187.5 eV, a step size of 1 eV, and a dwell time of 50 ms per step over 10 sweeps. These scans identified the presence of minor amounts of nitrogen (N) and sodium (Na), in addition to chromium (Cr), oxygen (O), and carbon (C). High-resolution scans of the O 1s (30 sweeps), Cr 2p (90 sweeps), and C 1s (30 sweeps) regions were obtained using a pass energy of 23 eV, a step size of 0.1 eV, and a dwell time of 50 ms per step. Sputter-depth profiles were recorded for 25 cycles by alternating sputtering the TDC surface at an angle of 45° with low energy 0.5 kV Ar+ ions over an area of 3 × 3 mm and recording scans of the C 1s, O 1s and Cr 2p peaks with a pass energy of 29.35 eV and a stepsize of 0.25 eV after every 12 s of sputtering during cycles 1 to 5, after every 24 s of sputtering during cycles 5 to 15 and after every 60 s during cycles 16 to 25. A low energy was used for the Ar+ ions in an attempt to minimize ion irradiation damage to the coating due to the sputtering. The sputtering rate at this energy, obtained from a polished 52100 sample, was +/- 0.25 nm/min. During the measurements, the chamber pressure remained at approximately 7.5 × 10⁻⁹ Torr due to the controlled inflow of argon ions for charge neutralization. The adventitious carbon C 1s peak, set at 284.8 eV, was used to charge-correct all recorded spectra. Data processing and interpretation were conducted using PHI Multipack software (version 9.9.2). The Strohmeier equation was applied to estimate the thickness of the passive film on the exposed surfaces, considering the predominant formation of Cr₂O₃ and Cr(OH)₃ [24]:

$$d = \lambda_{\text{oxorhy}}^{\text{Cr}} \sin\theta \ln \left[\frac{N_m^{\text{Cr}} \lambda_m^{\text{Cr}} I_{\text{oxorhy}}^{\text{Cr}}}{N_{\text{oxorhy}}^{\text{Cr}} \lambda_{\text{oxorhy}}^{\text{Cr}} I_m^{\text{Cr}}} + 1 \right] \quad (1)$$

All parameters of the equation can be described as follows: inelastic mean free paths of metallic Cr ($\lambda_m^{\text{Cr}} = 1.55$ nm), Cr(OH)₃ ($\lambda_{\text{hy}}^{\text{Cr}} = 2.27$ nm), and Cr₂O₃ ($\lambda_{\text{ox}}^{\text{Cr}} = 1.83$ nm), volume density of metal ($N_m^{\text{Cr}} = 7.19$ g/cm³), Cr(OH)₃ ($N_{\text{hy}}^{\text{Cr}} = 3.11$ g/cm³) and Cr₂O₃ ($N_{\text{ox}}^{\text{Cr}} = 5.22$ g/cm³), the peak fitted area percentages of the metallic Cr (I_m), Cr(OH)₃ ($I_{\text{hy}}^{\text{Cr}}$) and Cr₂O₃ ($I_{\text{ox}}^{\text{Cr}}$) signals, and the photoelectron take-off angle ($\theta = 45^\circ$ corresponding to 0.785 rad). The inelastic mean free paths of metallic chromium, oxide, and hydroxide were extracted from the NIST Electron Inelastic-Mean-Free-Path Database (SRD 71).

2.5. AC/DC Multi-Electrochemical analyses

Electrochemical measurements were conducted using a three-electrode setup with a Biologic SP 300 potentiostat. The reference electrode was Ag/AgCl/KCl_{3M} (+222 mV vs. SHE), the counter electrode was a platinum mesh, and the working electrodes were the TDC-coated samples. A 0.6 M NaCl solution, prepared with ultra-pure water (Milli-Q ix7003, resistivity > 5 MΩ.cm) and J.T.Baker™ NaCl, was used as the electrolyte to simulate an aggressive environment. The solution's pH at 22 ± 1 °C was measured as 5.6. Prior to measurements, the samples

were immersed in the electrolyte for 1 h to stabilize the open-circuit potential (OCP). Potentiodynamic polarization (PDP) was performed at a 1 mV/s scan rate, starting 100 mV below the OCP and extending to 1 V vs. Ag/AgCl. Electrochemical impedance spectroscopy (EIS) was conducted over a frequency range of 100 kHz to 10 mHz with a ± 10 mV sinusoidal perturbation.

To evaluate the electronic properties of the passive film on the TDC coating, Mott-Schottky (MS) analysis was conducted using multi-frequency EIS measurements [12,19]. The TDC sample was subjected to polarization in 50 mV potential increments, starting from 0 V and progressing to 1000 mV vs. Ag/AgCl, following a 1-hour exposure to a 3.5 wt% NaCl solution. During the measurements, an AC amplitude of ± 10 mV was applied. The Bode magnitude revealed a negative slope starting at approximately 6 kHz, indicating the onset of capacitive reactance influencing the polarization response. Consequently, 6 kHz was chosen as the reference frequency for the Mott-Schottky plot. The

MS measurements were interpreted using the following equation:

$$\frac{1}{C_{SC}^2} + \frac{1}{C_H^2} = -\frac{2}{\epsilon\epsilon_0 e N_A} \left(E - E_{fb} - \frac{kT}{e} \right) \quad (2)$$

here, C_{SC} represents the space charge capacitance, while C_H denotes the capacitance of the Helmholtz double layer. E is the applied potential, ϵ is the dielectric constant of the complex oxide film, and ϵ_0 is the vacuum permittivity ($8.854 \times 10^{-14} \text{F cm}^{-1}$). The electron charge is given by e ($1.6 \times 10^{-19} \text{C}$), N_A acceptor density, and E_{fb} is the flat band potential. Additionally, k and T represent the Boltzmann constant and absolute temperature, respectively. All samples were pre-cleaned in acetone for 2 min using a low-intensity ultrasonication process.

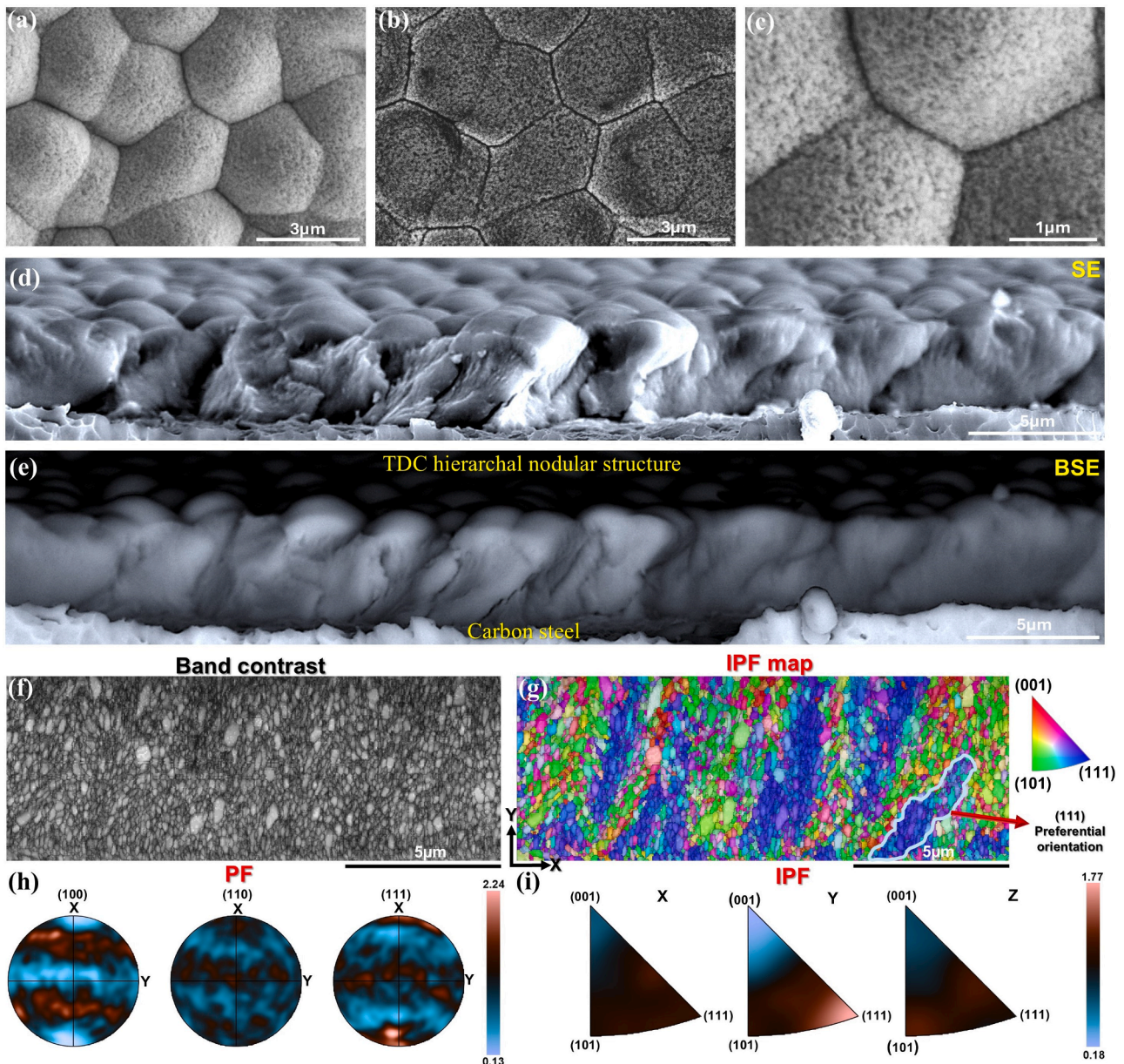


Fig. 1. (a–c) Top-view SEM images of the TDC coating surface at low and high magnifications, showing both secondary electron (SE) and backscattered electron (BSE) signals. (d, e) Cross-sectional SE and BSE-SEM images of the TDC coating were obtained by rupturing the coating to reveal the cross-section. Cross-sectional EBSD data of the mirror-polished TDC coating includes (f) band contrast, (g) inverse pole figure (IPF) color map, (h) pole figure, and (i) IPF orientation map.

3. Results and discussion

3.1. Microstructural characteristics of TDC coating

Fig. 1a–c present secondary electron (SE) and backscattered electron (BSE)-SEM top-view images of the TDC coating, illustrating its unique hierarchical nodular morphology across different magnifications. The nodules have an average diameter of $3.6 \pm 0.5 \mu\text{m}$ covering $\sim 95\%$ of the total surface area. The remaining $\sim 4\%$ corresponds to the boundaries, with a boundary length density of $0.61 \pm 0.02 \mu\text{m}/\mu\text{m}^2$. As shown in Fig. 1b, the backscatter signal captures the nodule distribution and its boundaries, revealing a defect-free surface with no signs of pinholes or micro-cracks. The SEM cross-sectional image of polished TDC coating presented in Fig. S1 clearly corroborates this observation. The cross-sectional SE and BSE-SEM images of the TDC coating, obtained by fracturing the material (Fig. 1d and e), show a uniform morphology, and a dense crystalline structure. Fig. 1f and g showcase the cross-sectional analysis of the TDC coating using electron backscatter diffraction (EBSD), including the band contrast and the inverse pole figure (IPF) color map. The utilization of EBSD facilitates a thorough assessment of the crystalline structure, grain size, and orientation, offering essential data to predict the physicochemical evolution at the metal/oxide/electrolyte interface, with direct implications for the corrosion process [25,26]. The band contrast image illustrates a near-nanocrystalline structure, characterized by an average grain size of $230 \pm 85 \text{ nm}$ and 86.5% of grain boundary angles greater than 10° . During the electrocrystallization process, the aggregation of grains creates multi-crystal branches, with polynear-nanograins coalescing and reorganizing

mostly along the (111) crystalline plane [27], as depicted in blue color in Fig. 1g. Besides, the pole figure (Fig. 1h) and IPF (Fig. 1i) demonstrate a wide-ranging distribution of grain orientations in the TDC coating cross-section, yet certain crystal branches are largely aligned with the $\langle 111 \rangle$ growth direction. EBSD data suggest that the near-nanocrystalline structure (reducing the grain size) can enhance the surface area-to-volume ratio by increasing the density of grain boundaries. This improvement, in turn, accelerates electrochemical oxidation kinetics and fosters the formation of stable passive nanofilms [28].

3.2. Analysis of surface chemical and oxidation state evolution using XPS

The near-nanocrystalline structure of the TDC coating promotes the formation of a bilayer surface oxide at the nanometer scale. Under extreme conditions, this bilayer oxide becomes increasingly pronounced, leading to its progressive growth and thickening over time. Hence, the native nano-oxide film on the fresh TDC surface was characterized after 7 days of exposure to 0.6 M NaCl using X-ray photoelectron spectroscopy (XPS). Fig. 2a and b depict high-resolution XPS spectra of Cr 2p and its corresponding O 1s signals, both for the fresh surface and after exposure conditions. Peak fitting of the Cr 2p spectra for both conditions revealed multiple components, including metallic Cr^0 , $\text{Cr}(\text{OH})_3$, and a range of Cr(III) species, each exhibiting the characteristic multiplet splitting of Cr^{3+} [29]. A sharply defined multiplet structure distinguishes Cr(III) oxides, whereas $\text{Cr}(\text{OH})_3$ is characterized by a broader, less clearly defined peak. The binding energy details for Cr 2p fitted peaks are summarized in Table S1. Additionally, across both exposed surfaces, a binding energy peak at 579.7 eV was remarked,

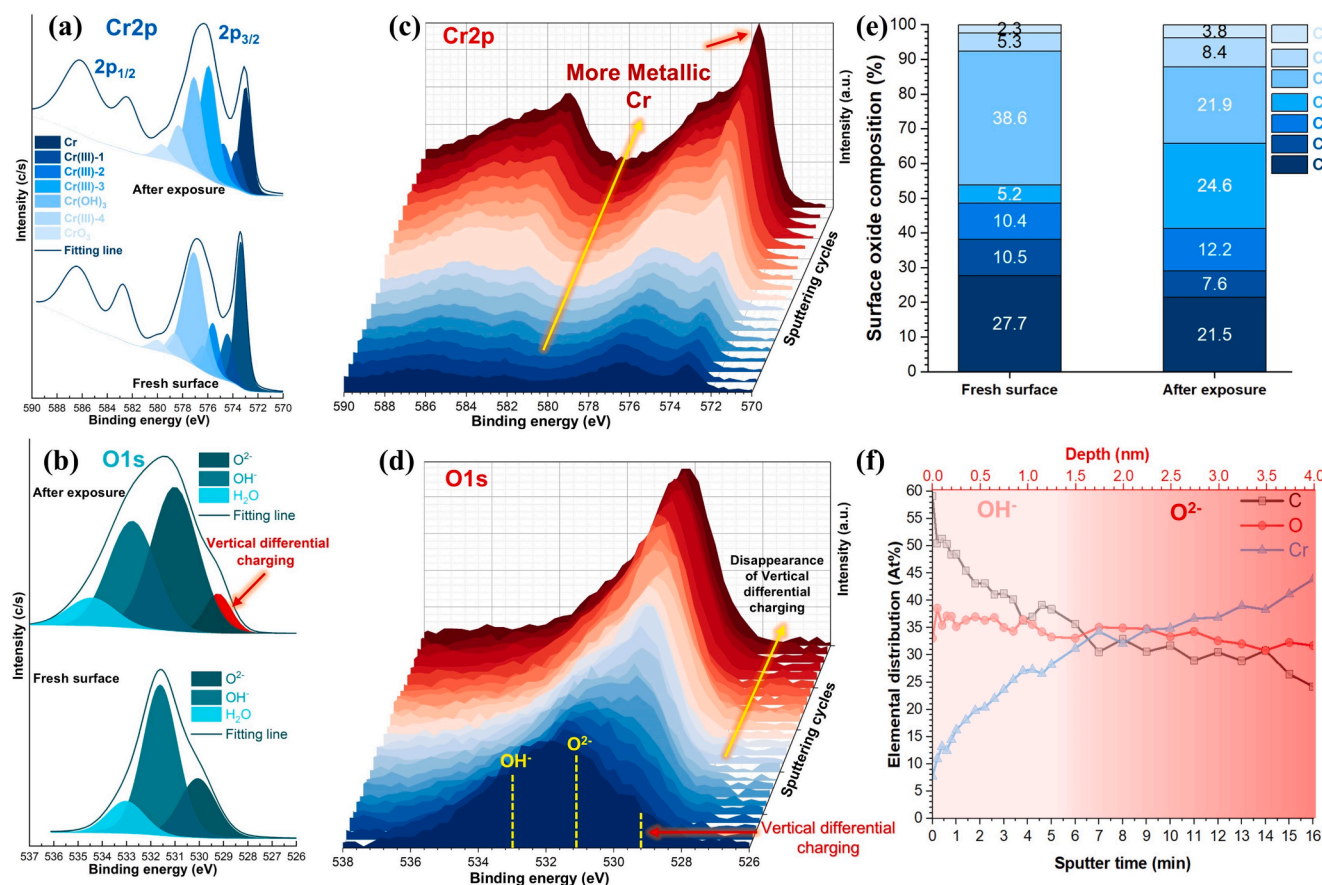


Fig. 2. XPS spectra for the TDC coating surface in the (a) Cr 2p and (b) O 1s electron energy regions were recorded under two conditions: the initial (fresh) surface and after 7 days of exposure to a 0.6 M NaCl solution. Stacked spectra for (c) Cr 2p and (d) O 1s regions were also acquired during Argon (Ar) sputtering of the TDC top surface. Panels (e) and (f) present, respectively, the relative percentages of various chromium oxidation states and the depth profiles of C, O, and Cr elements from the TDC surface layer. Note: The fitted OH^- peaks also include a minor contribution from oxygen-containing organic compounds.

which is characteristic of Cr(VI) compounds, such as CrO_3 , due to the lack of unpaired electrons [11]. Fig. 2a and e highlight the fitted peaks in the Cr 2p spectra for both the fresh surface and after exposure. A marked transformation in the relative proportions of various Cr(III) oxides with complex multiplet structures is observed. In particular, the decline in $\text{Cr}(\text{OH})_3$ and metallic Cr is evident after exposure to 0.6 M NaCl due to more surface oxidation and passive film growth. This is clearly demonstrated by the O 1s spectrum (Fig. 2b), where the TDC surface displays a significantly greater signal corresponding to lattice oxygen (O^{2-}) following exposure to 0.6 M NaCl. Besides, the observed shift in binding energy across all fitted O1s peaks after exposure, along with the appearance of a new peak at low binding energy, highlights the effect of vertical differential charging (Details regarding the binding energy of O1s fitted peaks can be found in Table S2). This can be attributed to two primary factors [30]. First, the charge gradient is initiated at the metal/oxide interface, which acts as the origin of a natural dipole moment. This dipole moment, associated with the metal/oxide interface, generates the observed charge gradient. Second, this effect stems from the capacitive properties of the non-conductive nano-oxide film and the interfacial layer situated between the metal (here near-nanocrystalline structure) and the oxide film.

The TDC passive film on the fresh surface has an estimated thickness of 1.7 nm for $\text{Cr}(\text{OH})_3$ and 1.3 nm for Cr_2O_3 , analyzed from Fig. 2a. After 7 days of exposure to 0.6 M NaCl, the thickness decreased to 1.5 nm for $\text{Cr}(\text{OH})_3$ and increased to 2.2 nm for Cr_2O_3 . The XPS sputter-depth profiles of Cr2p and O1s (from TDC exposed to 0.6 M NaCl for 7 days) highlight the changes in the bilayer nano-oxide film (Fig. 2c and d). The spectra reveal that the outer layer, dominated by $\text{Cr}(\text{OH})_3$, gradually diminishes with sputtering, while the inner Cr_2O_3 layer becomes increasingly apparent (Fig. 2d), suggesting a dynamic evolution between hydroxide and oxide phases (Fig. 2f). With further sputtering a progression toward the Cr metallic/ bilayer oxide interface is made, as evidenced by the metallic Cr peak increasing in intensity (Fig. 2c), confirming the presence of a very thin passive film. The higher surface

non-conductivity or charge transfer resistance arises from the extensive formation of Cr(III) oxides with complex multiplet structures that are characterized by their significant band gap energies (3.4 eV for Cr_2O_3 and 2.4 eV for $\text{Cr}(\text{OH})_3$ [31]) and associated work function [2].

3.3. Electrochemical interactions and corrosion behavior of TDC coating

To assess the electrochemical activity, bilayer nano-oxide film barrier properties, and corrosion resistance of TDC coating in 0.6 M NaCl, a multi-method approach combining AC and DC techniques was used. These methods included cyclic potentiodynamic polarization (PDP), electrochemical impedance spectroscopy (EIS), and Mott-Schottky analysis obtained from dynamic EIS measurements (Fig. 3a–c). In the cyclic PDP during the forward scan or with increasing overpotential, the TDC surface initially exhibits a small activation region, followed by a transition into the passivation region, and ultimately reaches the transpassive region, with an onset potential of 570 mV vs. Ag/AgCl. This process is characterized by a progressive increase in dissolution, which becomes the dominant mechanism, along with concurrent passivation at the nodule boundaries, as illustrated by the SEM images in Fig. S2. A notable feature is the very small hysteresis loop, suggesting that the onset of pitting or preferential dissolution at the nodules' boundaries begins at 735 mV vs. Ag/AgCl. During the forward overpotential scan, the corrosion current density (i_{corr}) was $8.2 \text{ nA} \cdot \text{cm}^{-2}$, and the corrosion potential (E_{corr}) was -180 mV vs. Ag/AgCl. Conversely, in the reverse scan, the corrosion current density increased to $78.2 \text{ nA} \cdot \text{cm}^{-2}$, while the corrosion potential shifted to -618 mV vs. Ag/AgCl. The increase of 800 mV vs. Ag/AgCl in E_{corr} and the nearly tenfold rise in i_{corr} highlight the formation of a durable and compact bilayer oxide film (higher E_{corr}). However, the slight boundary damage to the nodule (lower i_{corr}) suggests localized susceptibility, likely attributed to its high-energy sites (Fig. S2).

The Mott-Schottky analysis presented in Fig. 3b reveals the presence of a bilayer nano-oxide structure, characterized by a negative slope in

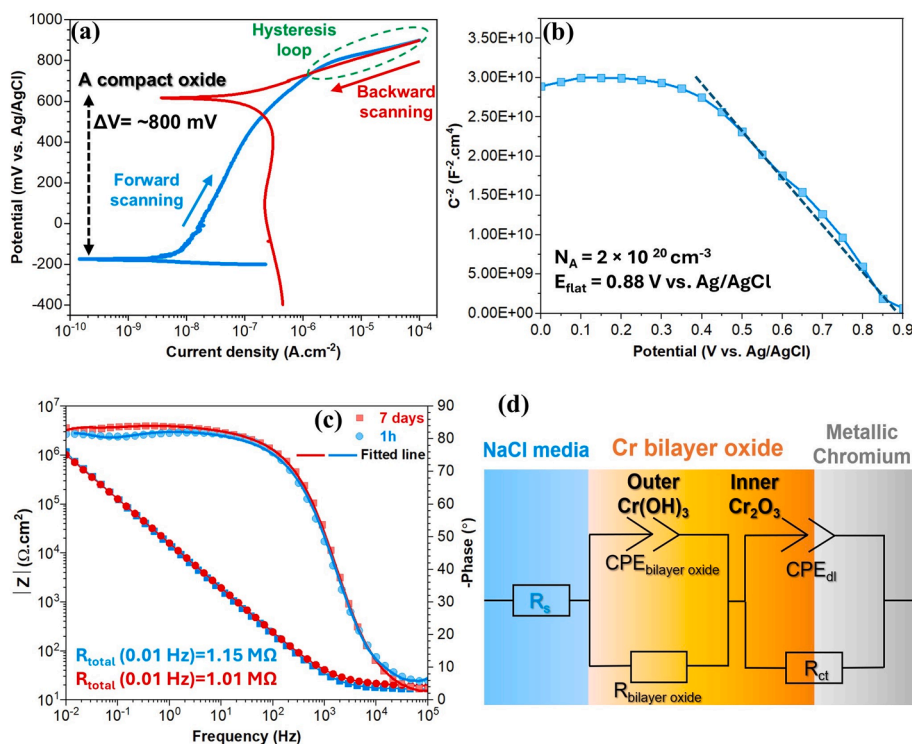


Fig. 3. (a) Cyclic voltammogram (logarithmic scale) of the TDC coating following 1 h OCP monitoring in 0.6 M NaCl solution. (b) Mott-Schottky analysis of the TDC coating after 1 h exposure to 0.6 M NaCl solution. (c) Bode phase and amplitude plots of the TDC coating after 1 h and 7 days of exposure to 0.6 M NaCl solution. (d) The electrical equivalent circuit (EEC) model was applied for the precise fitting of the TDC EIS curves.

the plot, which is indicative of p-type semiconductor behavior (e.g., indicative of acceptor density [32,33]. This demonstrates that Cr^{3+} vacancies are the primary point defects in the oxide film [13]. Under elevated anodic overpotentials exceeding 0.8 V vs. Ag/AgCl, the minimum C^{-2} value primarily arises from the transpassive conversion of Cr (III) into Cr(IV) and Cr(VI) [34], predominantly originating at the nodule boundaries. The analysis highlights a lower p-type charge carrier density ($N_A = 2 \times 10^{20} \text{ cm}^{-3}$) and a flat band potential of 0.88 V vs. Ag/AgCl, indicating a reduced number of charge carriers for electrochemical activities and enhanced chemical stability of the bilayer oxide. The Bode phase and amplitude plots in Fig. 3c reveal a consistently high phase angle (-82° and -85°) and an exceptionally stable total impedance ($R_{\text{total}}(1\text{h}) = 1.15 \text{ M}\Omega$ and $R_{\text{total}}(7 \text{ days}) = 1.01 \text{ M}\Omega$) for the TDC surface, both after 1 h and 7 days of exposure to a 0.6 M NaCl solution. Fig. 3d presents the most suitable equivalent electrical circuit (EEC) for the system, indicating that the TDC coating exhibits two distinct time-constant elements (Fitting results are available in Table S3). These elements suggest a bilayer of compact oxides, consisting of a $\text{Cr}(\text{OH})_3$ /

electrolyte interface and a multi-oxide structure (identified by XPS as a multiplet of Cr(III)) at the Cr_2O_3 /near-nanocrystalline Cr interface. It is worth highlighting again that the exceptional polarization resistance of the TDC coating stems from its near-nanocrystalline structure, characterized by a high density of grain boundaries plus excellent non-conductivity properties of bilayer nano-oxide. Indeed, these grain boundaries, serving as diffusion pathways, facilitate the rapid formation of a robust, dense, and non-conductive oxide layer, thereby improving the coating's protective effectiveness [35]. Consistent with the XPS results, the observed vertical differential charging at the oxide/air interface and the high polarization resistance at the metal/oxide/liquid interface are attributed to the non-conductive bilayer nano-oxide and the high charge transfer resistance (R_{ct}) at the metal/oxide interface.

3.4. Analysis of surface topography and electrical surface potential evolution using AFM and SKPFM

To investigate the TDC coating's surface attributes, including its

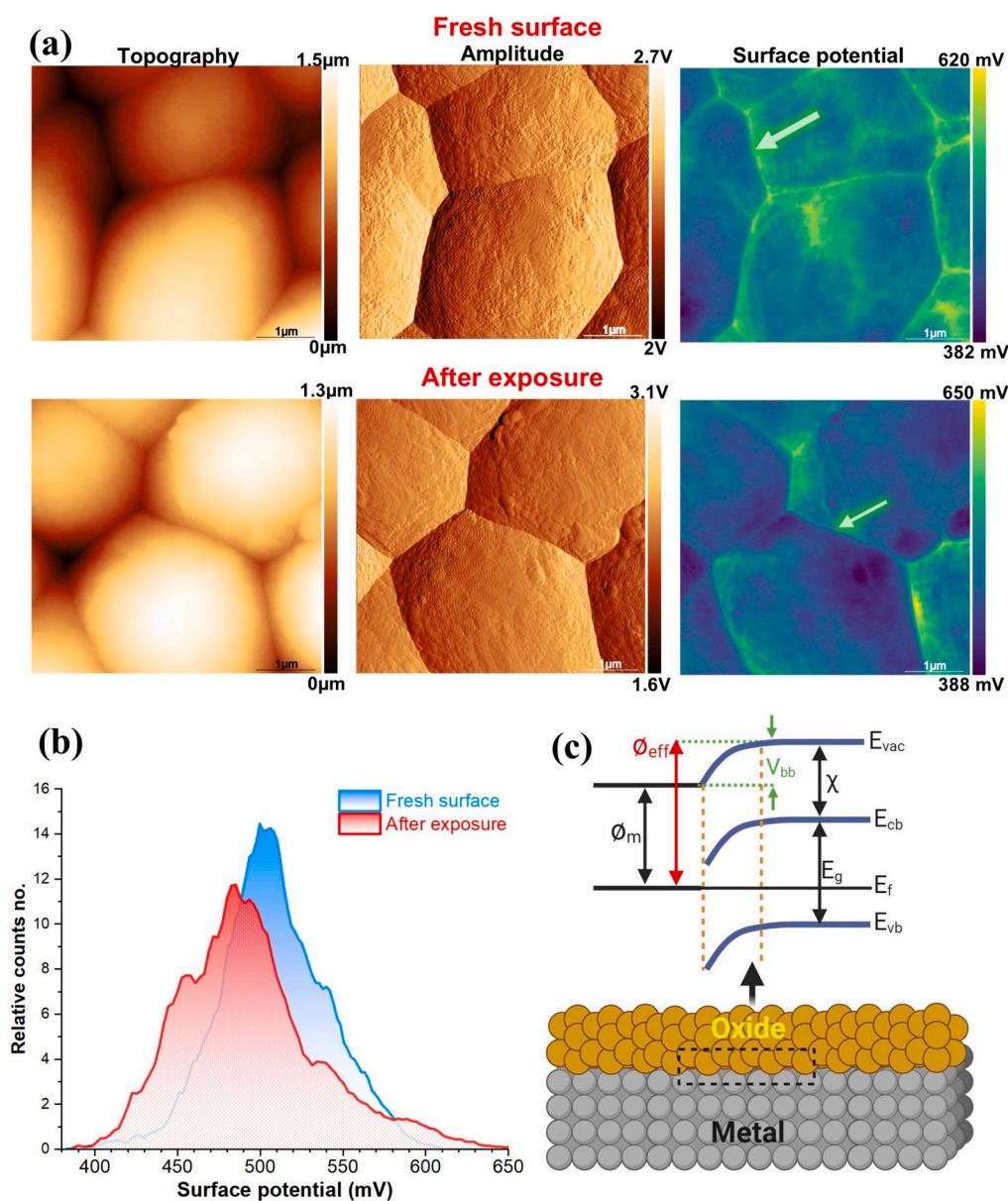


Fig. 4. (a) Topography, amplitude, and electrical surface potential maps of the TDC coating on a fresh surface and following 7 days exposure to 0.6 M NaCl solution. (b) Surface potential histograms corresponding to the maps in (a). (c) Schematic representation of energy level alignment and band bending at the metal/oxide interface.

physical and electrical properties, particularly after exposure to 0.6 M NaCl, topography, amplitude, and electrical potential/charge maps were recorded, see Fig. 4a. The combined analysis of local topography and amplitude mappings provides a precise depiction of the nodules on the TDC coating surface, revealing their nuanced height differences and the pattern of boundary distribution (more visible in amplitude). While surface oxidation of the nodules is difficult to discern through topography and amplitude signals, SKPFM surface-sensitive analysis distinctly highlighted variations in the electrical surface potential between the TDC nodules and their boundaries, both in their fresh state and after exposure. Surface potential maps indicate increased surface potential and/or charge distribution at the boundaries of the nodules and their surrounding regions, which diminishes after 7 days of exposure to 0.6 M NaCl (indicated by arrows in maps). In fact, the localized charge accumulation at the nodule boundaries can give rise to defect states, which subsequently alter the energy levels and create a contact potential difference (ΔCPD) within the space charge regions at these boundaries [36,37]. The surface potential histogram in Fig. 4b highlights a heterogeneous distribution of surface potential and/or charge, with a noticeable shift toward lower values following exposure to the solution. This shift suggests a decrease in surface charge and an increase in surface potential, particularly in terms of the work function due to more surface oxidation [38].

Overall, when dealing with a metallic surface covered by an oxide layer, the electronic properties of the nanometer oxide film, including its type (p- or n-type semiconductor), band gap, dipoles, as well as the positions of occupied and unoccupied states, and the presence of vacancies (e.g., oxygen or cation vacancies), significantly affect the local electrical surface potential [39]. As a result, the work function (WF) of oxidation states is higher than those of pure metal (ϕ_m) [40] (Fig. 4c). In particular, at the oxide/metal interface, the vacuum level (E_{vac}) on the oxide side shifts to a higher value, accompanied by a slight misalignment. The degree of this misalignment, including the band bending (V_{bb}) at the metal/oxide interface, is determined by the magnitude of the interfacial dipole moment. This observation gives rise to the concept of a new work function parameter, known as the effective work function (ϕ_{eff}), as shown in Fig. 4c and the following equation [41]:

$$\phi_{\text{eff}} = \chi + E_g + (E_f - E_{\text{vb}}) \quad (3)$$

where χ is electron affinity, E_g , E_f , E_{cb} , and E_{vb} are band-gap energy, Fermi level, conduction band, and valence bands, respectively. The increased formation of bilayer nano-oxide structures results in a more non-conductive surface oxide layer (more multiplet of Cr(III) than Cr(OH)₃), as demonstrated by the vertical differential charging peak in XPS analysis. Discontinuities or defects at the interface of near-nanocrystalline (especially high grain boundaries) and bilayer nano-oxide structures can introduce extra energy barriers, impeding charge transfer and resulting in localized charge trapping or scattering [39,41]. This phenomenon is coupled with a decrease in charge carrier density within the passive film, as observed through Mott-Schottky plots. The trend is further validated by a significant rise in charge transfer resistance (R_{ct}) at the near-nanocrystalline/bilayer nano-oxide interface, as measured by EIS. This consistency is further corroborated by local SKPFM, which reveals a notable reduction in surface charge and an increase in the effective work function (ϕ_{eff}) [39,42].

4. Conclusions

To summarize, we visualized with multiple characterization techniques how a nodular thin dense chromium (TDC) coating offers exceptional corrosion resistance following exposure to NaCl solution, primarily due to its dense near-nanocrystalline structure and the formation of a protective and non-conductive bilayer surface oxide. XPS results revealed vertical differential charging, attributed to the capacitive properties of both nonconductive Cr(OH)₃ and the multiple

oxidation states of Cr³⁺ that developed within the nano-thin oxide film and the dense, near-nanocrystalline chromium structure (TDC coating). EIS analysis further reinforces this finding by revealing a markedly high total charge resistance at the metallic Cr/bilayer oxide interface. Finally, the SKPFM mappings and histogram data indicated a decline in the electrical surface potential and charge distribution of TDC nodules upon exposure to NaCl solution, most notably at the nodule boundaries, a result of increased passivation and an elevated effective work function.

5. Contribution

E. Rahimi conceived the idea and guided the project. T. Nijdam performed the XPS characterization and the following discussion. A. Jahagirdar supported and prepared all coating samples. Both E. Broitman and A. Mol supervised the project, discussed the results, and revised the manuscript. All authors wrote the manuscript and contributed to the overall scientific interpretation.

CRediT authorship contribution statement

Ehsan Rahimi: Writing – review & editing, Writing – original draft, Visualization, Validation, Methodology, Investigation, Formal analysis, Data curation, Conceptualization. **Thijs Nijdam:** Writing – review & editing, Investigation, Formal analysis, Data curation. **Adwait Jahagirdar:** Writing – review & editing, Data curation. **Esteban Broitman:** Writing – review & editing, Visualization, Validation, Supervision, Resources, Conceptualization. **Arjan Mol:** Writing – review & editing, Visualization, Validation, Supervision, Resources, Funding acquisition, Conceptualization.

Declaration of competing interest

The authors declare that they have no known competing financial interests or personal relationships that could have appeared to influence the work reported in this paper.

Acknowledgments

This research was carried out under project number T23011 in the framework of the Research Program of the Materials innovation institute (M2i) (www.m2i.nl) and was funded by Holland High Tech | TKIHOSTM via the PPS allowance scheme for public-private partnerships.

Appendix A. Supplementary material

Supplementary data to this article can be found online at <https://doi.org/10.1016/j.apsusc.2025.162504>.

Data availability

Data will be made available on request.

References

- [1] F. Presuel-Moreno, M.A. Jakab, N. Tailleart, M. Goldman, J.R. Scully, Corrosion-resistant metallic coatings, *Mater. Today* 11 (2008) 14–23.
- [2] E. Rahimi, R. Sanchis-Gual, X. Chen, A. Imani, Y. Gonzalez-Garcia, E. Asselin, A. Mol, L. Fedrizzi, S. Pané, M. Lekka, Challenges and strategies for optimizing corrosion and biodegradation stability of biomedical micro- and nanoswimmers: a review, *Adv. Funct. Mater.* 33 (2023) 2210345.
- [3] E. McCafferty, *Introduction to Corrosion Science*, Springer, 2010.
- [4] N. Wint, A. de Vooy, H. McMurray, The corrosion of chromium based coatings for packaging steel, *Electrochim. Acta* 203 (2016) 326–336.
- [5] J.M. Prabhakar, R.S. Varanasi, C.C. da Silva, S. Saood, A. de Vooy, A. Erbe, M. Rohwerder, Chromium coatings from trivalent chromium plating baths: characterization and cathodic delamination behaviour, *Corros. Sci.* 187 (2021) 109525.

- [6] H. Ramezani-Varzaneh, S. Allahkaram, M. Isakhani-Zakaria, Effects of phosphorus content on corrosion behavior of trivalent chromium coatings in 3.5 wt.% NaCl solution, *Surf. Coat. Technol.* 244 (2014) 158–165.
- [7] N. Imaz, M. Ostra, M. Vidal, J. Díez, M. Sarret, E. García-Lecina, Corrosion behaviour of chromium coatings obtained by direct and reverse pulse plating electrodeposition in NaCl aqueous solution, *Corros. Sci.* 78 (2014) 251–259.
- [8] B.O. Okonkwo, C. Jeong, H.B. Lee, C. Jang, E. Rahimi, A. Davoodi, Development and optimization of trivalent chromium electrodeposit on 304L stainless steel to improve corrosion resistance in chloride-containing environment, *Heliyon* 9 (2023).
- [9] Y. Tian, Q. Yang, W. Li, Y. Gong, Q. Zhao, C. Li, X. Sheng, Anti-corrosion applications of 2D transition metal based layered materials, *Materials, Advances* 5 (2024) 2655–2667.
- [10] L.-N. Zhang, X.-L. Xiong, Y. Yan, K.-W. Gao, L.-J. Qiao, Y.-J. Su, Atomic modeling for the initial stage of chromium passivation, *Int. J. Miner. Metall. Mater.* 26 (2019) 732–739.
- [11] M.C. Biesinger, B.P. Payne, A.P. Grosvenor, L.W. Lau, A.R. Gerson, R.S.C. Smart, Resolving surface chemical states in XPS analysis of first row transition metals, oxides and hydroxides: Cr, Mn, Fe, Co and Ni, *Appl. Surf. Sci.* 257 (2011) 2717–2730.
- [12] J. León, S. Pletincx, H. Terryn, B. Özkaya, E. García-Lecina, J. Vega, Unravelling the Fe effect on the corrosion of chromium coatings: chemical composition and semiconducting properties, *J. Electrochem. Soc.* 168 (2021) 121501.
- [13] S. Marcelin, B. Ter-Ovanesian, B. Normand, Electronic properties of passive films from the multi-frequency Mott–Schottky and power-law coupled approach, *Electrochem. Commun.* 66 (2016) 62–65.
- [14] J. Yang, P. Ji, J. Zhang, W. Xu, J. Jiao, Y. Lian, L. Jiang, B. Zhang, Effect of current density on the texture, residual stress, microhardness and corrosion resistance of electrodeposited chromium coating, *Surf. Coat. Technol.* 471 (2023) 129868.
- [15] Y. Wang, Y. Liu, G. Li, M. Zheng, Y. Li, A. Zhang, Y. Zhang, Microstructure and flow accelerated corrosion resistance of Cr coatings electrodeposited in a trivalent chromium bath, *Surf. Coat. Technol.* 422 (2021) 127527.
- [16] J. Hu, Y. Zhang, X. Yang, H. Li, H. Xu, C. Ma, Q. Dong, N. Guo, Z. Yao, Effect of pack-chromizing temperature on microstructure and performance of AISI 5140 steel with Cr-coatings, *Surf. Coat. Technol.* 344 (2018) 656–663.
- [17] J. Whiteside, A.C. de Vooyo, E. Sackett, H.N. McMurray, Influence of uniaxial deformation on surface morphology and corrosion performance of chromium-based coatings for packaging steel, *Corros. Sci.* 190 (2021) 109662.
- [18] B. Weiss, A. Lefebvre, O. Sinot, M. Marquer, A. Tidu, Effect of grinding on the sub-surface and surface of electrodeposited chromium and steel substrate, *Surf. Coat. Technol.* 272 (2015) 165–175.
- [19] J. León, B. Ter-Ovanesian, B. Normand, H. Terryn, B. Özkaya, M. Lekka, H.-J. Grande, E. García-Lecina, J. Vega, Corrosion resistance of electroplated coatings based on chromium trivalent-baths, *Surf. Coat. Technol.* 481 (2024) 130616.
- [20] Broitman, E. Coatings to Improve Bearing Performance. *Evolution* 2022, 1–7, in: Available online: <https://evolution.skf.com/coatings-to-improve-bearing-performance/>.
- [21] SKF Coatings, in: S. Group (Ed.), 2020. Available online: https://cdn.skfmediahub.skf.com/api/public/0901d19680a4e17f/pdf_preview_medium/0901d19680a4e17f_pdf_preview_medium.pdf.
- [22] J. Beswick, A. Voskamp, J. vd Sanden, M. Verburgh, S. Horton, Bearing material/treatment developments at the SKF engineering and research centre, in: *Creative use of bearing steels*, ASTM International, 1993.
- [23] SKF. Kaydon Endurakote®—Plated Bearings. *Kaydon Bearing Solutions—SKF*, in: Available online: https://www.kaydonbearings.com/Endurakote_bearings.htm &r=1.
- [24] M.C. Biesinger, B.P. Payne, L.W.M. Lau, A. Gerson, R.S.C. Smart, X-ray photoelectron spectroscopic chemical state quantification of mixed nickel metal, oxide and hydroxide systems, *Surf. Interf. Anal.* 41 (2009) 324–332.
- [25] J.J. Gray, B.S. El Dasher, C.A. Orme, Competitive effects of metal dissolution and passivation modulated by surface structure: an AFM and EBSD study of the corrosion of alloy 22, *Surf. Sci.* 600 (2006) 2488–2494.
- [26] X. Fu, Y. Ji, X. Cheng, C. Dong, Y. Fan, X. Li, Effect of grain size and its uniformity on corrosion resistance of rolled 316L stainless steel by EBSD and TEM, *Mater. Today Commun.* 25 (2020) 101429.
- [27] M. Sun, H.-G. Liao, K. Niu, H. Zheng, Structural and morphological evolution of lead dendrites during electrochemical migration, *Sci. Rep.* 3 (2013) 3227.
- [28] R.K. Gupta, N. Birbilis, The influence of nanocrystalline structure and processing route on corrosion of stainless steel: a review, *Corros. Sci.* 92 (2015) 1–15.
- [29] B. Payne, M. Biesinger, N. McIntyre, X-ray photoelectron spectroscopy studies of reactions on chromium metal and chromium oxide surfaces, *J. Electron Spectrosc. Relat. Phenom.* 184 (2011) 29–37.
- [30] B. Vincent Crist, XPS guide for insulators: Electron flood gun operation and optimization, surface charging, controlled charging, differential charging, useful FWHMs, problems and solutions, and advice, *J. Vac. Sci. Technol. A* 42 (2024).
- [31] G. Tranchida, M. Clesi, F. Di Franco, F. Di Quarto, M. Santamaria, Electronic properties and corrosion resistance of passive films on austenitic and duplex stainless steels, *Electrochim. Acta* 273 (2018) 412–423.
- [32] R. Auguste, H.L. Chan, E. Romanovskaia, J. Qiu, R. Schoell, M.O. Liedke, M. Butterling, E. Hirschmann, A.G. Attallah, A. Wagner, F.A. Selim, D. Kaoumi, B. P. Uberuaga, P. Hosemann, J.R. Scully, A multimodal approach to revisiting oxidation defects in Cr₂O₃, *npj Mater. Degrad.* 6 (2022) 61.
- [33] A.M. Oje, A.A. Ogwu, Chromium oxide coatings with the potential for eliminating the risk of chromium ion release in orthopaedic implants, *R. Soc. Open Sci.* 4 (2017) 170218.
- [34] D.-S. Kong, S.-H. Chen, C. Wang, W. Yang, A study of the passive films on chromium by capacitance measurement, *Corros. Sci.* 45 (2003) 747–758.
- [35] A. Fattah-Alhosseini, O. Imantalab, G. Ansari, The role of grain refinement and film formation potential on the electrochemical behavior of commercial pure titanium in Hank's physiological solution, *Mater. Sci. Eng. C* 71 (2017) 827–834.
- [36] T.-X. Qin, E.-M. You, M.-X. Zhang, P. Zheng, X.-F. Huang, S.-Y. Ding, B.-W. Mao, Z.-Q. Tian, Quantification of electron accumulation at grain boundaries in perovskite polycrystalline films by correlative infrared-spectroscopic nanoimaging and Kelvin probe force microscopy, *Light Sci. Appl.* 10 (2021) 84.
- [37] M. Mousavi, E. Rahimi, J.M.C. Mol, Y. Gonzalez-Garcia, The effect of phosphorus content on the microstructure and localised corrosion of electroless nickel-coated copper, *Surf. Coat. Technol.* 492 (2024) 131174.
- [38] M.T. Greiner, L. Chai, M.G. Helander, W.-M. Tang, Z.-H. Lu, Transition metal oxide work functions: the influence of cation oxidation state and oxygen vacancies, *Adv. Funct. Mater.* 22 (2012) 4557–4568.
- [39] E. Rahimi, A. Imani, M. Lekka, F. Andreatta, Y. Gonzalez-Garcia, J.M.C. Mol, E. Asselin, L. Fedrizzi, Morphological and surface potential characterization of protein nanobiofilm formation on magnesium alloy oxide: their role in biodegradation, *Langmuir* 38 (2022) 10854–10866.
- [40] M.T. Greiner, Z.-H. Lu, Thin-film metal oxides in organic semiconductor devices: their electronic structures, work functions and interfaces, *NPG Asia Mater.* 5 (2013) e55–e.
- [41] H. Zhu, R. Ramprasad, Effective work function of metals interfaced with dielectrics: A first-principles study of the Pt-HfO₂ interface, *Phys. Rev. B* 83 (2011) 081416.
- [42] E. Rahimi, D. Kim, R. Offoiaich, R. Sanchis-Gual, X.-Z. Chen, P. Taheri, Y. Gonzalez-Garcia, J.M.C. Mol, L. Fedrizzi, S. Pané, M. Lekka, Biodegradation of oxide nanoparticles in apoferritin protein media: a systematic electrochemical approach, *Adv. Mater. Interf.* 10 (2023) 2300558.